Deformation induced pseudomagnetic fields in complex carbon architectures

R. Gupta,[1,*] S. Maisel,[2] F. Rost,[1] D. Weckbecker,[1] M. Fleischmann,[1] H. Soni,[3] S. Sharma,[4] A. Görling,[2] and S. Shallcross[1,†]

[1]*Lehrstuhl für Theoretische Festkörperphysik, Staudtstr. 7-B2, 91058 Erlangen, Germany*

[2]*Lehrstuhl für Theoretische Chemie, Egerlandstr. 3, 91058 Erlangen, Germany*

[3]*School of Sciences, Indrashil University, Mehsana Dist., Gujarat, 382740 India*

[4]*Max-Born-Institute for Nonlinear Optics, Max-Born-Straße 2A, 12489 Berlin, Germany*

(Received 26 May 2019; published 23 August 2019)

We show that the physics of deformation in α-, β-, and 6, 6, 12-graphyne is, despite their significantly more complex lattice structures, remarkably close to that of graphene, with inhomogeneously strained graphyne described at low energies by an emergent Dirac-Weyl equation augmented by strain induced electric and pseudomagnetic fields. To show this, we develop a continuum theory of deformation in these materials, and consider two versions of this theory: (i) a truncated theory describing only the low-energy degrees of freedom of the conical intersection, which thus is spinor valued as in graphene, and (ii) one describing the full sublattice space. The spinor valued continuum theory agrees very well with the full continuum theory at low energies, showing that the remarkable physics of deformation in graphene generalizes to these more complex carbon architectures. In particular, we find that deformation induced pseudospin polarization and valley current loops, key phenomena in the deformation physics of graphene, both have their counterpart in these more complex carbon materials.

DOI: 10.1103/PhysRevB.100.085135

I. INTRODUCTION

One of the most remarkable features of graphene is the robustness of its ultrarelativistic low-energy physics. The Dirac-Weyl Hamiltonian that describes the quasiparticles of pristine graphene remains a valid description even under substantial deformation, simply being augmented by effective pseudomagnetic and electric fields that encode the deformation in a low-energy description. These fields, except for the requirement that the pseudomagnetic field change sign at conjugate valleys, behave exactly as physical electric and magnetic fields [1,2], resulting in a rich phenomenology of deformation induced physics in single layer graphene. For realistic strain the induced magnetic field can reach hundreds of tesla, a remarkable effect observable as deformation induced Landau levels in graphene [3]. This deep connection between structural deformation and an induced electromagnetic field promises a control over electronic properties unrivaled in any three dimensional material, and generates novel physical effects such as deformation induced valley filters [4–8], and psuedospin polarization [9,10].

Following the experimental realization of graphene low-energy conical intersections have been predicted for several all-carbon materials, each with a substantially more complex lattice structure than that of graphene [11–41]. For example, 6, 6, 12-graphyne and β-graphyne both possess 18 carbon atoms in their unit cell, as opposed to the two atom unit cell honeycomb lattice of graphene. This entails a much more difficult chemistry of their fabrication [12,42,43], but also a fundamental difference in the low-energy physics. In graphene, the sublattice space is isomorphic to SU(2) pseudospin space, and it is this that underpins the connection between deformation and effective electric and magnetic fields. However, this simple relation between the pseudospin and sublattice degrees of freedom is lost in these more complex materials. While the structural physics of nonuniform deformation in the graphynes has been quite intensively investigated [24,27,36,40], corresponding attention has not been devoted to the electronic theory of general nonuniform deformations, with most electronic investigations focusing either on uniform uniaxial and biaxial strains [13,22,37–39,44,45], "rotating" strain [18], or phononic excitations [46]. A natural question is therefore: how much of the rich electronic physics of nonuniform deformation in graphene finds a counterpart in these more complex carbon architectures?

The purpose of the present paper is to answer this question. To that end, we generalize the continuum theory of deformation in graphene to materials with arbitrary numbers of atoms in the unit cell. As a minimal description of the electronic structure entails one π-orbital per basis atom, this theory can now exist in two forms: one involving all sublattice degrees of freedom, and a downfolded theory describing only the spinor degree of freedom of the low-energy Dirac cone. For all three graphynes, we find that this latter description is, at low energies, in very close agreement with the full continuum theory. Thus the intimate connection between structure and effective electromagnetic field is preserved in these more complex architectures, and the rich physics of deformation in graphene generalizes to the semimetallic graphynes.

*Current address: School of Physics, HH Wills Laboratory, Tyndall Avenue BS8 1TL, United Kingdom.

†sam.shallcross@fau.de

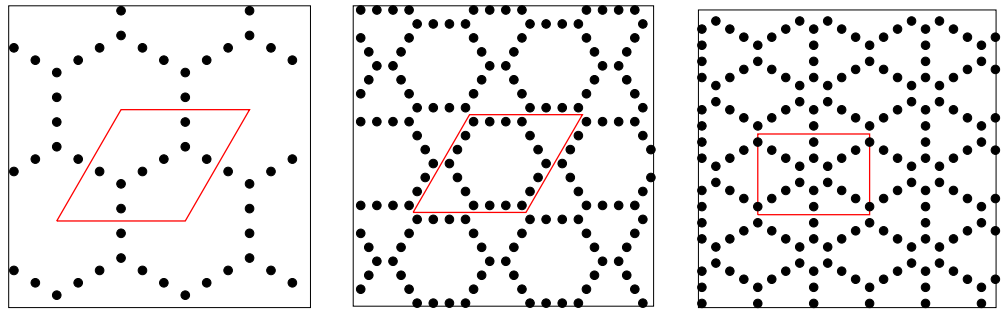

FIG. 1. Lattice structures of α-graphyne, β-graphyne, and 6,6,12-graphyne, with the unit cell indicated by the red (light shaded) box.

II. CONTINUUM THEORY OF COMPLEX CARBON MATERIALS

While the continuum theory of deformation in graphene is very well developed, the same attention has not been paid to the graphynes. The complex lattice structures of these materials (see Fig. 1) render the methods used in deriving the continuum theory of deformation for graphene either prohibitively cumbersome (the expansion of a tight-binding Hamiltonian) or inapplicable (transport of the Dirac-Weyl equation to nonMinkowski metric). To avoid this we employ a methodology [47–52] based on an exact map of the tight-binding Hamiltonian to a general continuum operator, recently used to treat stacking deformations in bilayer structure [48,51,52], and acoustic and optical deformations in single-layer graphene [47]. We first briefly review this theory, before extending it to include a treatment of currents, and subsequently describing both the complete and downfolded versions required to investigate deformation in graphyne.

A. An exact map of the tight-binding Hamiltonian

In this approach, the "input" consists simply of a hopping function envelope $t_{\alpha\beta}(\mathbf{r}, \boldsymbol{\delta})$ describing the tight-binding hopping matrix amplitude from a position $\mathbf{r}$ on sublattice α to $\mathbf{r}+\boldsymbol{\delta}$ on sublattice β in the material, with the change in electron hopping due to deformation encoded in the $\mathbf{r}$ dependence of this function. The tight-binding Hamiltonian is therefore

$$H_{\mathrm{TB}} = \sum_{\alpha\mathbf{R}_i\beta\mathbf{R}_j} t_{\alpha\beta}(\mathbf{R}_i+\boldsymbol{\nu}_\alpha, \mathbf{R}_j+\boldsymbol{\nu}_\beta-\mathbf{R}_i-\boldsymbol{\nu}_\alpha) \times c^\dagger_{\mathbf{R}_j+\boldsymbol{\nu}_\beta\beta} c_{\mathbf{R}_i+\boldsymbol{\nu}_\alpha\alpha}, \quad (1)$$

where $\mathbf{R}_i$ and $\boldsymbol{\nu}_\alpha$ are the lattice and basis vectors of the underlying high-symmetry lattice.

The corresponding continuum Hamiltonian $H(\mathbf{r}, \mathbf{p})$ that is exactly equivalent to this tight-binding Hamiltonian is given by [50]

$$[H(\mathbf{r}, \mathbf{p})]_{\alpha\beta} = \frac{1}{V_{\mathrm{UC}}} \sum_j M_{j\alpha\beta}\eta_{\alpha\beta}(\mathbf{r}, \mathbf{K}_j+\mathbf{p}/\hbar), \quad (2)$$

where V_{UC} is the unit cell volume, the sum is over all $\mathbf{G}_j$ vectors of the reciprocal lattice, $\mathbf{K}_j = \mathbf{K}_0 + \mathbf{G}_j$ with $\mathbf{K}_0$ a reference momentum in the Brillouin zone (for the graphynes, we study this will be the momentum at which the conical intersection occurs),

$$\eta_{\alpha\beta}(\mathbf{r}, \mathbf{q}) = \int d\boldsymbol{\delta}\, e^{-i\mathbf{q}\cdot\boldsymbol{\delta}} t_{\alpha\beta}(\mathbf{r}, \boldsymbol{\delta}) \quad (3)$$

the so-called mixed space hopping function, with the M_j matrices are given by

$$M_{j\alpha\beta} = e^{i\mathbf{G}_j\cdot(\boldsymbol{\nu}_\alpha-\boldsymbol{\nu}_\beta)}. \quad (4)$$

As shown in Ref. [47] expansion of the $\mathbf{r}$ dependence of $\eta_{\alpha\beta}(\mathbf{r}, \mathbf{q})$ for slowly varying deformations and expansion of the $\mathbf{p}$ dependence for momenta near the conical intersection leads to a systematic treatment of deformation within the continuum picture.

B. An exact map of the current operator

In this work, a focus will be on the valley current densities induced by deformation, and thus we require a current operator corresponding to the Hamiltonian (2). The current operator in tight-binding theory, the so-called bond current operator, is given by [53,54]

$$\mathbf{j}(\mathbf{R}_i) = \frac{1}{2V_{\mathrm{UC}}} \sum_\alpha [n(\mathbf{R}_i+\boldsymbol{\nu}_\alpha)\mathbf{v} + \mathbf{v}n(\mathbf{R}_i+\boldsymbol{\nu}_\alpha)], \quad (5)$$

where $\hat{n}(\mathbf{R}_i+\boldsymbol{\nu}_\alpha) = |\mathbf{R}_i+\boldsymbol{\nu}_\alpha\rangle\langle\mathbf{R}_i+\boldsymbol{\nu}_\alpha|$ is the density operator with the velocity operator

$$\mathbf{v} = \frac{1}{i\hbar}[\mathbf{r}, H(\mathbf{r}, \mathbf{p})], \quad (6)$$

[with $H(\mathbf{r}, \mathbf{p})$ the Hamiltonian of Eq. (2)] and where we have included normalization by the unit cell volume $1/V_{\mathrm{UC}}$.

One would expect that the method used to derive Eq. (2) from Eq. (1) should, if applied to Eq. (5), yield a current density given by

$$\mathbf{j}(\mathbf{r}) = \tfrac{1}{2}(\Psi(\mathbf{r})^\dagger[\nabla_{\mathbf{p}}H\Psi(\mathbf{r})] + [\nabla_{\mathbf{p}}H\Psi(\mathbf{r})]^\dagger\Psi(\mathbf{r})) \quad (7)$$

with $H(\mathbf{r}, \mathbf{p})$ given by Eq. (2), i.e., in the continuum limit the relation between Hamiltonian and current operator should follow from Hamilton's equations. However, given the very different forms of the tight-binding Hamiltonian (1) and the bond-current operator (5) in tight-binding theory it is not obvious that this is the case.

Indeed, the precise link between the tight-binding and continuum limits of the current operator has been the subject of recent discussion in the context of recovering the Schödinger current operator from the bond current formulas [53] for a

quadratic band model. As noted in Ref. [53] the fundamental difficultly involves taking the continuum limit of a discrete grid and the associated ambiguity in the definition of differential operators. Employing the same methodology involved in the derivation of Eq. (2), however, we find a general form for the continuum current operator precisely equivalent to the general tight-binding bond-current formula while avoiding all use of grid limits. This turns out to be just the intuitive result given by Eq. (7) from which we can then recover, as specific cases, both the Schrödinger and Dirac-Weyl current operators.

To derive this result, we first consider the matrix element of Eq. (5) with a general state of the system

$$|\Psi\rangle = \sum_{\mathbf{k}_1\alpha} c_{\mathbf{k}_1\alpha}\big|\Phi_{\mathbf{k}_1\alpha}\big\rangle, \tag{8}$$

where $|\Phi_{\mathbf{k}_1\alpha}\rangle$ denotes a Bloch function of sublattice α and crystal momentum $\mathbf{k}_1$:

$$\big|\Phi_{\mathbf{k}_1\alpha}\big\rangle = \frac{1}{\sqrt{N}}\sum_{\mathbf{R}_i} e^{i\mathbf{k}_1\cdot(\mathbf{R}_i+\boldsymbol{\nu}_\alpha)}|\mathbf{R}_i+\boldsymbol{\nu}_\alpha\rangle, \tag{9}$$

where $|\mathbf{R}_i+\boldsymbol{\nu}_\alpha\rangle$ represents a local orbital at position $\mathbf{R}_i+\boldsymbol{\nu}_\alpha$. One finds for the matrix element $\langle\Psi|\mathbf{j}(\mathbf{R}_i)|\Psi\rangle$ the result

$$\frac{1}{2V_{\mathrm{UC}}}\sum_{\mathbf{k}_1,\mathbf{k}_2,\alpha',\beta}\Big[c^*_{\mathbf{k}_1\alpha'}c_{\mathbf{k}_2\beta}\big\langle\Phi_{\mathbf{k}_1\alpha'}|\hat{n}(\mathbf{R}_i+\nu_\alpha)\hat{\mathbf{v}}|\Phi_{\mathbf{k}_2\beta}\big\rangle + \mathrm{H.c.}\Big]. \tag{10}$$

We now work out the matrix element $\langle\Phi_{\mathbf{k}_1\alpha'}|\hat{n}(\mathbf{R}_i+\nu_\alpha)\hat{\mathbf{v}}|\Phi_{\mathbf{k}_2\beta}\rangle$ in detail. Insertion of the Bloch functions, Eq. (9), yields

$$\frac{-i}{N\hbar}\sum_{\mathbf{R}_j} e^{-i\mathbf{k}_1\cdot(\mathbf{R}_i+\boldsymbol{\nu}_\alpha)}e^{i\mathbf{k}_2\cdot(\mathbf{R}_j+\boldsymbol{\nu}_\beta)}[\mathbf{R}_i+\boldsymbol{\nu}_\alpha-\mathbf{R}_j-\boldsymbol{\nu}_\beta] \times t_{\alpha\beta}(\mathbf{R}_i+\boldsymbol{\nu}_\alpha,\mathbf{R}_j+\boldsymbol{\nu}_\beta), \tag{11}$$

where $t_{\alpha\beta}(\mathbf{R}_i+\boldsymbol{\nu}_\alpha,\mathbf{R}_j+\boldsymbol{\nu}_\beta)=\langle\mathbf{R}_i+\boldsymbol{\nu}_\alpha|H|\mathbf{R}_j+\boldsymbol{\nu}_\beta\rangle$ is the usual tight-binding hopping matrix element. To derive a continuum limit we now employ the Poisson sum formula in the form

$$\sum_{\mathbf{R}_j} f(\mathbf{R}_j+\boldsymbol{\nu}_\beta) = \frac{1}{V_{\mathrm{UC}}}\sum_{\mathbf{G}_j}\hat{f}(\mathbf{G}_j)e^{i\mathbf{G}_j\cdot\boldsymbol{\nu}_\beta} \tag{12}$$

for which the appropriate function $f(\mathbf{r})$ is

$$f(\mathbf{r}) = e^{i\mathbf{k}_2\cdot\mathbf{r}}(-\mathbf{r})t_{\alpha\beta}(\mathbf{R}_i+\boldsymbol{\nu}_\alpha,\mathbf{r}) \tag{13}$$

with the Fourier transform

$$\hat{f}(\mathbf{q}) = \int d\mathbf{r}\, e^{-i(\mathbf{q}-\mathbf{k}_2)\cdot\mathbf{r}}(-\mathbf{r})t_{\alpha\beta}(\mathbf{R}_i+\boldsymbol{\nu}_\alpha,\mathbf{r}). \tag{14}$$

Evaluation of the integral and employing the Poisson sum in Eq. (11) then yields

$$\frac{e^{i(\mathbf{k}_2-\mathbf{k}_1).(\mathbf{R}_i+\boldsymbol{\nu}_\alpha)}}{V\hbar}\sum_{\mathbf{G}_j} e^{i\mathbf{G}_j\cdot(\boldsymbol{\nu}_\alpha-\boldsymbol{\nu}_\beta)}\nabla_{\mathbf{k}_2}t_{\alpha\beta}(\mathbf{R}_i+\boldsymbol{\nu}_\alpha,\mathbf{k}_2+\mathbf{G}_j), \tag{15}$$

where $V=NV_{\mathrm{UC}}$ is the system volume. By defining a reference momenta $\mathbf{K}_0$ through $\mathbf{k}_2+\mathbf{G}_j=\mathbf{G}_j+\mathbf{K}_0+\mathbf{p}_2$ and promotion of $\mathbf{p}_2$ to an operator, this expression can straightforwardly be recast into a form involving the continuum Hamiltonian $H(\mathbf{r},\mathbf{p})$, Eq. (2),

$$\frac{1}{\sqrt{V}}e^{-i\mathbf{p}_1\cdot\mathbf{r}}\{\nabla_{\mathbf{p}}H_{\alpha\beta}(\mathbf{r},\mathbf{p})\}\frac{1}{\sqrt{V}}e^{i\mathbf{p}_2\cdot\mathbf{r}}. \tag{16}$$

To complete the transformation to the continuum description we introduce the vector plane waves

$$\phi_{\mathbf{p}_1\alpha}(\mathbf{r}) = \frac{1}{\sqrt{V}}e^{i\mathbf{p}_1\cdot\mathbf{r}}|\alpha\rangle, \tag{17}$$

where $|\alpha\rangle$ represents a unit vector in a space of dimension equal to the number of atomic degrees of freedom (for graphene these would just be pseudospin up and pseudospin down states). Employing these functions, we then arrive at the desired operator equivalence:

$$\big\langle\Phi_{\mathbf{k}_1\alpha}|\hat{n}(\mathbf{r})\hat{\mathbf{v}}|\Phi_{\mathbf{k}_2\beta}\big\rangle = \phi^\dagger_{\mathbf{p}_1\alpha}(\mathbf{r})\big[\nabla_{\mathbf{p}}H(\mathbf{r},\mathbf{p})\phi_{\mathbf{p}_2\beta}(\mathbf{r})\big]. \tag{18}$$

Insertion of this result back into Eq. (10) and the obvious definition for the system wave function in the continuum representation as

$$\Psi(\mathbf{r}) = \sum_{\mathbf{p}_1} c_{\mathbf{p}_1\alpha}\phi_{\mathbf{p}_1\alpha}(\mathbf{r}) \tag{19}$$

then leads to our final result

$$\Psi(\mathbf{r})^\dagger\mathbf{j}\Psi(\mathbf{r}) = \tfrac{1}{2}(\Psi(\mathbf{r})^\dagger[\nabla_{\mathbf{p}}H\Psi(\mathbf{r})] + [\nabla_{\mathbf{p}}H\Psi(\mathbf{r})]^\dagger\Psi(\mathbf{r})), \tag{20}$$

which is evidently the sought for intuitive form given by Eq. (7).

This expression trivially reproduces both the well known current operators for the Dirac-Weyl and Schrödinger equation. For a Schrödinger form $H=\frac{1}{2m}p^2$, we find

$$\mathbf{j}(\mathbf{r}) = \frac{1}{2m}[\Psi(\mathbf{r})^*\mathbf{p}\Psi(\mathbf{r}) - \Psi(\mathbf{r})\mathbf{p}\Psi(\mathbf{r})^*], \tag{21}$$

whereas for the Dirac-Weyl Hamiltonian $H=v_F\boldsymbol{\sigma}\cdot\mathbf{p}$, we have

$$\mathbf{j}(\mathbf{r}) = \Psi(\mathbf{r})^\dagger v_F\boldsymbol{\sigma}\Psi(\mathbf{r}). \tag{22}$$

There is, however, an important caveat to Eq. (20). While the bond current operator always satisfies a discrete form of the continuity equation appropriate for the tight-binding Hamiltonian [54,55] for the continuum version of the bond current, Eq. (20), this is not guaranteed. This follows as Eq. (20) is simply the expectation value of the velocity operator and, curiously, it turns out that Eq. (20) does violate the continuity equation, but only for Hamiltonians containing a higher than second power in momentum [56]. As shown in Appendix, the Dirac-Weyl theory of deformation in graphene satisfies the continuity equation up to $O(p^2)$, including all "acoustic" field terms (both gauge terms and so-called "geometric" terms, the corresponding Fermi velocity terms, and trigonal warping correction terms), see also Ref. [57]. Effective Hamiltonians with a momentum power greater than 2 are, however, a common occurrence in condensed matter. To that end, other less intuitive definitions of the current operator that do satisfy the continuity equation have been provided [58–60], and these can encode nonclassical current contributions. Nevertheless, the breakdown of a classical relationship between velocity and current should probably be viewed as a failure of effective Hamiltonian theory.

TABLE I. Tight-binding parametrization of the form $A\exp(-B\boldsymbol{\delta}^2)$, with the value of A is given in the table (in eV) and for each material and bond type, and B taken to be 30.03, 10.03, and 20.00 eV/Å for, respectively, α-graphyne, β-graphyne, and 6,6,12-graphyne (i.e. the same for all bond types). Following Ref. [19], we also introduce a second parameter for the graphene-acetylene hopping in 6,6,12-graphyne (denoted t' in that work) for which we take the value -4.17 eV/Å.

Material	graphene	acetylene	graphene-acetylene
α-graphyne	-3.02	-3.02	-3.02
β-graphyne	-4.30	-2.00	-2.70
6,6,12-graphyne	-2.50	-6.25	-2.95

III. CONTINUUM THEORY OF α-,β-, AND 6, 6, 12-GRAPHYNE

A. Tight-binding parameterization

A continuum theory of the pristine lattices, i.e., without deformation, is easily obtained from Eq. (2). In this case the mixed space hopping function, Eq. (3), loses its $\mathbf{r}$ dependence becoming simply the Fourier transform of the electron hopping function defined between each sublattice: $\hat{t}_{\alpha\beta}(\mathbf{q}) = \int d\boldsymbol{\delta}\, e^{-i\mathbf{q}\cdot\boldsymbol{\delta}} t_{\alpha\beta}(\boldsymbol{\delta})$. We therefore require a functional form of $t_{\alpha\beta}(\boldsymbol{\delta})$ describing electron hopping for the three graphynes we consider: α-, β-, and 6, 6, 12-graphyne. We base our prameterization on the tight-binding parameters of Ref. [19], which are defined only for the nearest-neighbor hopping, and fit these to a Gaussian functional form

$$t(\boldsymbol{\delta}^2) = A\exp(-B\boldsymbol{\delta}^2) \tag{23}$$

such that the nearest-neighbor hopping is reproduced, with negligible next nearest (and further) hopping, see Table I.

While the precise functional form of the hopping envelope is immaterial, this Gaussian form is useful as (i) it renders the Fourier transform straightforward and rapidly convergent [a hopping form $A\exp(-B|\mathbf{r}|)$ would produce a numerically inconvenient algebraic decay in the Fourier transform] and (ii) deformation, which modifies the hopping matrix element through changes of the hopping vector, is easily included. The tight-binding band structures using this parametrization are shown as the full lines in Fig. 2. The expected low-energy conical intersections are found (i) at the K point for α-graphyne [20], (ii) on the line connecting the Γ and M points for β-graphyne [20], and (iii) two low-energy cones one at the X point (we denote this cone I) and a second on the line connecting Γ and Y points (denoted cone II) for 6, 6, 12-graphyne [20]. In fact, cone I is shifted somewhat further off the X point as compared to *ab initio* calculations [20] (a line fraction of 0.2 as opposed to 0.08), and cone II somewhat closer to the Γ point (a line fraction of 0.5 as opposed to 0.62 in *ab initio*). Furthermore, with only nearest-neighbor hopping the cone tilting found in *ab initio* for β-graphyne and cone II in 6, 6, 12-graphyne is not reproduced. We find that lowering the value of B somewhat in Eq. (23), to increase next-nearest-neighbor strength, restores the cone tilting. We have checked that sensible variation of the tight-binding parameters does not qualitatively change the results and conclusions we present in subsequent sections for nonuniform deformation in these materials.

B. Continuum theory for pristine lattices

To extract a tractable continuum description from Eq. (2) requires a Taylor expansion in momentum about the Dirac point. Expanding the hopping function in Eq. (2) to first order

$$\hat{t}_{\alpha\beta}(\mathbf{K}_j + \mathbf{p}) \approx \hat{t}_{\alpha\beta}\left(\mathbf{K}_j^2\right) + \mathbf{p}\cdot\boldsymbol{\nabla}_{\mathbf{q}}\hat{t}_{\alpha\beta}(\mathbf{q}^2)\big|_{\mathbf{q}=\mathbf{K}_j} \tag{24}$$

generates an expression of the form

$$H_0^{\text{full}}(\mathbf{p}) = H^{(0)} + H_x^{(1)}p_x + H_y^{(1)}p_y, \tag{25}$$

where the Hamiltonian at the Dirac momenta is

$$H_{\alpha\beta}^{(0)} = \frac{1}{V_{\text{UC}}}\sum_j M_{\alpha\beta j}\hat{t}_{\alpha\beta}^{(0)}\left(\mathbf{K}_j^2\right) \tag{26}$$

and the matrices $H_i^{(1)}$ given by

$$\left[H_i^{(1)}\right]_{\alpha\beta} = \frac{2}{V_{\text{UC}}}\sum_j M_{\alpha\beta j}\hat{t}_{\alpha\beta}^{(1)}\left(\mathbf{K}_j^2\right)K_{ji}, \tag{27}$$

where K_{ji} is the ith component of the vector $\mathbf{K}_j$. The matrices (26) and (27) are labeled by sublattice indices, i.e., represent 8×8 matrices for α-graphyne and 18×18 matrices for β-graphyne and 6, 6, 12-graphyne. These therefore describe not

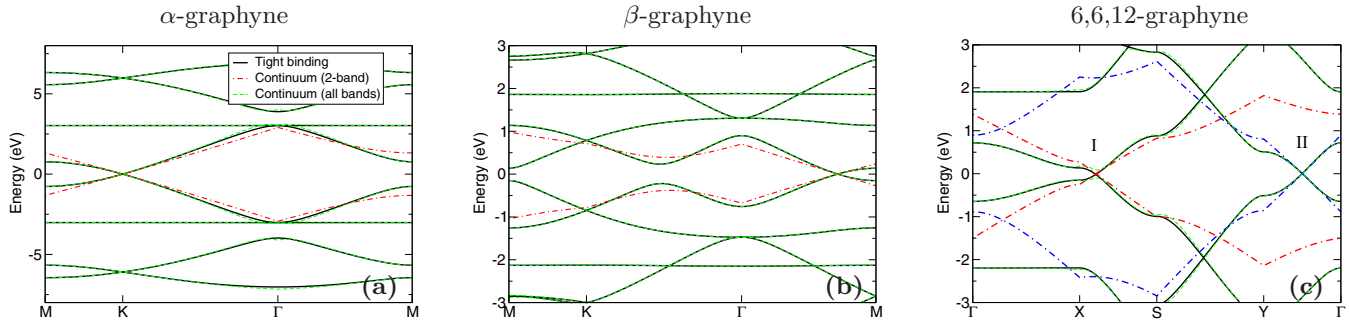

FIG. 2. Tight-binding band structures (full line, black online) of (a) α-graphyne, (b) β-graphyne, and (c) 6,6,12-graphyne. Shown also are the band structure generated by two continuum approximations; one designed to reproduce the low-energy Dirac-Weyl conical intersection (dot-dashed lines, red and blue curves online) and one designed to reproduce all bands (dashed lines, green online). Both these continuum theories include only up to second order in momentum. In (c), the expansion point for the all-band continuum description is the Dirac point of cone II although, as can be observed, this generates a reasonable agreement even close to cone I.

only the low-energy conical intersection (described generically by a spinor degree of freedom) but also all other band manifolds. In Fig. 2, is shown the band structure obtained from Eq. (25), with additionally second order in momentum terms included, revealing an excellent agreement with the underlying tight-binding method.

To obtain a description of the low-energy conical intersection, we must downfold the full continuum theory. To that end, we diagonalize the Hamiltonian at the Dirac point $H^{(0)}$, Eq. (26), and apply the resulting unitary transformation U to the full Hamiltonian $H_0^{\text{full}}(\mathbf{p})$. This yields

$$H = \boldsymbol{\epsilon} + UH_x^{(1)}U^\dagger p_x + UH_y^{(1)}U^\dagger p_y, \tag{28}$$

where $\boldsymbol{\epsilon}$ is a diagonal matrix whose entries are the eigenvalues at the Dirac point momenta, with the matrices $H^{(1)}$ now encoding hybridization of these bands at a finite momentum away from the Dirac point. This now allows us to identify the subspace corresponding to degenerate eigenvalues at the Dirac point, and by retaining only this subspace one arrives at a spinor valued low-energy Hamiltonian. This procedure yields a Dirac-Weyl form, but with an SU(2) rotation. Undoing this with a further unitary transform U_s we then find a generic final form for all three materials [11,14]

$$H_0(\mathbf{p}) = v_x\sigma_x p_x + v_y\sigma_y p_y + (t_x p_x + t_y p_y)\sigma_0. \tag{29}$$

The band structure calculated using Eq. (29) is shown as the dot-dashed lines in Fig. 2, showing good agreement with the full tight-binding calculation for the low-energy conical intersection. Further improvement requires additional bands to be included in the continuum theory, not higher orders of momenta.

While Eq. (29) provides a good description of the low-energy manifold it does not directly provide the physical wave function; for this a back transformation is required. Given a spinor eigenvector ϕ of Eq. (29), we must firstly transform back to the global SU(2) frame

$$c = U_s\phi, \tag{30}$$

which then provides the coefficients for constructing the physical wave function from the Dirac point wave functions:

$$\Psi_i = \sum_{j\in\text{low}} c_j U_{ij}, \tag{31}$$

where Ψ_i is the ith component of the physical wave function (i.e., in sublattice space) while the sum j is over the band indices of the low-energy manifold (recall that U is the unitary transform that diagonalizes H_0 the Hamiltonian at the Dirac point momenta). In graphene such a back transformation is, of course, unnecessary; a low-energy expansion directly yields a Dirac-Weyl equation. For any more complex material, however, the coefficients of the Dirac-Weyl spinor wave function merely parametrize the low-energy conical intersection in terms of the Dirac point wave functions.

C. Continuum theory of deformation

Inclusion of deformation into the low-energy scheme requires describing how electron hopping changes throughout the material, i.e., the full function $t_{\alpha\beta}(\mathbf{r}, \boldsymbol{\delta})$. This can be obtained simply from the geometric information of how the deformation changes the hopping $\boldsymbol{\delta}$ at point $\mathbf{r}$ in the material, via substitution of $\boldsymbol{\delta}$ in the hopping function of the high-symmetry material $t_{\alpha\beta}(\boldsymbol{\delta})$ by $t_{\alpha\beta}(\boldsymbol{\delta}(\mathbf{r}))$. The change in the square of the hopping vector due to the applied deformation field $\mathbf{u}(\mathbf{r})$ is just

$$\boldsymbol{\delta}^2 \to (\boldsymbol{\delta} + \mathbf{u}(\mathbf{r}+\boldsymbol{\delta}) - \mathbf{u}(\boldsymbol{\delta}))^2, \tag{32}$$

which, upon substitution into a hopping function $t_{\alpha\beta}(\boldsymbol{\delta}^2)$ yields, via a Taylor expansion for slowly varying fields, the mixed space hopping function

$$\begin{aligned}\eta_{\alpha\beta}(\mathbf{r},\mathbf{q}) = {}& \hat{t}^{(0)}_{\alpha\beta}(\mathbf{q}^2) + \hat{t}^{(1)}_{\alpha\beta}(\mathbf{q}^2)\big(\varepsilon_{xx}(\mathbf{r}) + \tfrac{1}{2}(\partial_x\mathbf{u}(\mathbf{r}))^2\big)q_x^2 \\ & + \hat{t}^{(1)}_{\alpha\beta}(\mathbf{q}^2)\big(\varepsilon_{yy}(\mathbf{r}) + \tfrac{1}{2}(\partial_y\mathbf{u}(\mathbf{r}))^2\big)q_y^2 \\ & + \hat{t}^{(1)}_{\alpha\beta}(\mathbf{q}^2)(2\varepsilon_{xy}(\mathbf{r}) + \partial_x\mathbf{u}(\mathbf{r})\cdot\partial_y\mathbf{u}(\mathbf{r}))q_xq_y.\end{aligned} \tag{33}$$

In this expression, $\varepsilon_{ij} = \frac{1}{2}(\partial_i u_j + \partial_j u_i)$ and $t^{(n)}_{\alpha\beta}(\mathbf{q}^2)$ is the Fourier transform of the nth order derivative of the high-symmetry hopping function:

$$t^{(n)}_{\alpha\beta}(\mathbf{q}^2) = \int d\boldsymbol{\delta} e^{i\boldsymbol{\delta}\cdot\mathbf{q}} \frac{\partial^n t(\boldsymbol{\delta}^2)}{\partial(\boldsymbol{\delta}^2)^n}. \tag{34}$$

Insertion of this result directly into Eq. (2) leads to a Hamiltonian of the form

$$\begin{aligned}H^{\text{full}}_{\text{def}} = {}& H_{xx}\big(\varepsilon_{xx} + \tfrac{1}{2}(\partial_x\mathbf{u})^2\big) + H_{yy}\big(\varepsilon_{yy} + \tfrac{1}{2}(\partial_y\mathbf{u})^2\big) \\ & + H_{xy}(2\varepsilon_{xy}(\mathbf{r}) + \partial_x\mathbf{u}(\mathbf{r})\cdot\partial_y\mathbf{u}(\mathbf{r}))\end{aligned} \tag{35}$$

with the matrices H_{nm} given by

$$[H_{nm}]_{\alpha\beta} = \frac{1}{V_{\text{UC}}}\sum_j M_{\alpha\beta j}\hat{t}^{(0)}_{\alpha\beta}(\mathbf{K}_j^2)K_{jn}K_{jm}, \tag{36}$$

where again K_{jn} is the nth component of the vector $\mathbf{K}_j = \mathbf{K}_0 + \mathbf{G}_j$. This along with Eq. 25 provides a continuum description in which all bands are included, i.e., in terms of all sublattice degrees of freedom.

To identify the low-energy sector of the Hamiltonian with deformation, we employ the same transformations U and U_s that yielded the low-energy sector for the pristine lattice. This, for all three materials, then results in the following generic form for the low-energy deformation Hamiltonian

$$\begin{aligned}H_{\text{def}}(\mathbf{r},\mathbf{p}) = {}& \big[\varepsilon_{xx} + \tfrac{1}{2}(\partial_x\mathbf{u})^2\big](\sigma_0 f_{xx} + \sigma_x g_{xx}) \\ & + \big[\varepsilon_{yy} + \tfrac{1}{2}(\partial_y\mathbf{u})^2\big](\sigma_0 f_{yy} + \sigma_x g_{yy}) \\ & + [2\varepsilon_{xy} + \partial_x\mathbf{u}\cdot\partial_y\mathbf{u})](\sigma_y g_{xy})\end{aligned} \tag{37}$$

where we have suppressed the $\mathbf{r}$ dependence in the deformation tensor and fields, and where the f_{ij} and g_{ij} are constants. This is very close to the form of deformation in graphene, which can be obtained by substituting $f_{xx} = f_{yy} = \alpha$ and $g_{xx} = -g_{yy} = -g_{xy} = \beta$ into this expression. This latter condition,

$$g_{xx} = -g_{yy} = -g_{xy}, \tag{38}$$

will hold for all materials in which the Dirac cone is protected by symmetry, as this ensures that scaling the lattice constant cannot displace the Dirac cone off the high-symmetry point. This is true for α-graphyne, and we find Eq. (38) to be exactly satisfied by our deformation expansion, but not for β- or 6, 6, 12-graphyne. For these materials, biaxial deformation

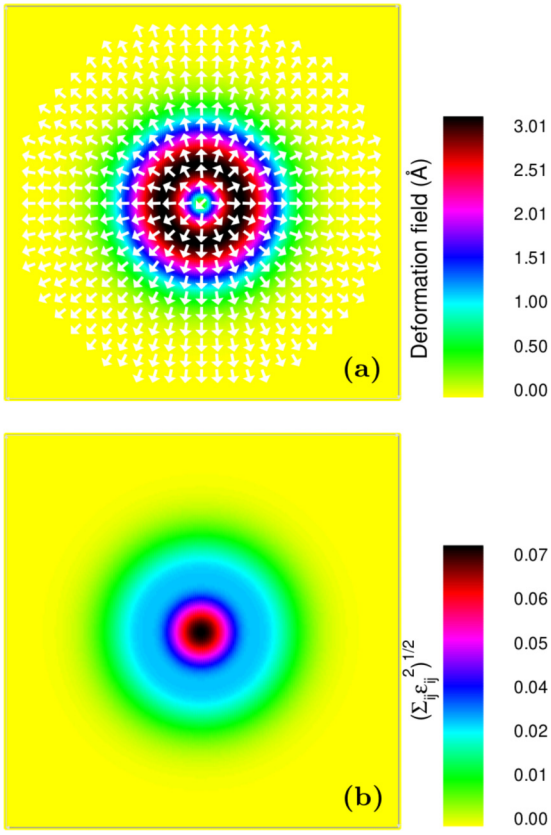

FIG. 3. The in-plane deformation applied to all materials; the length scale of the unit cell is 100a in all cases. In (a), is shown the deformation field with the color bar the magnitude and the arrow the direction, while in (b), is shown the magnitude of the deformation tensor ϵ.

shifts the Dirac cone in momentum space; for β-graphyne towards the X point, while for 6, 6, 12-graphyne, cone I moves towards the X point and cone II towards the Y point [45].

IV. ELECTRONIC STRUCTURE OF NONUNIFORM DEFORMATION IN GRAPHYNE

Having established the basic theory we now examine the electronic consequences of nonuniform deformation. After a brief description of the numerical methodology, we first examine the robustness of the low-energy conical manifolds under deformation, before considering the changes in electron densities and current densities induced by deformation.

A. Numerical details

Solution of either the two-band or full band Hamiltonian with deformation, Eqs. (35) and (37), is performed using a basis of eigenstates from the pristine system. For a momentum $\mathbf{k}_0$ the basis set is formed from all eigenstates of the pristine system with momenta $|\mathbf{k} - \mathbf{k}_0| < k_{\rm cut}$ and energy $|\epsilon^{(0)}_{\mathbf{k}i}| < e_{\rm cut}$. The advantage of this basis lies in the efficiency of convergence: we find that typically to converge the electronic structure in an energy window E requires $e_{\rm cut} \approx 1.5E$. The basis size is determined by $e_{\rm cut}$ with $k_{\rm cut}$ chosen so as the restrict the calculation to a single valley. We find that $e_{\rm cut}$ chosen so that

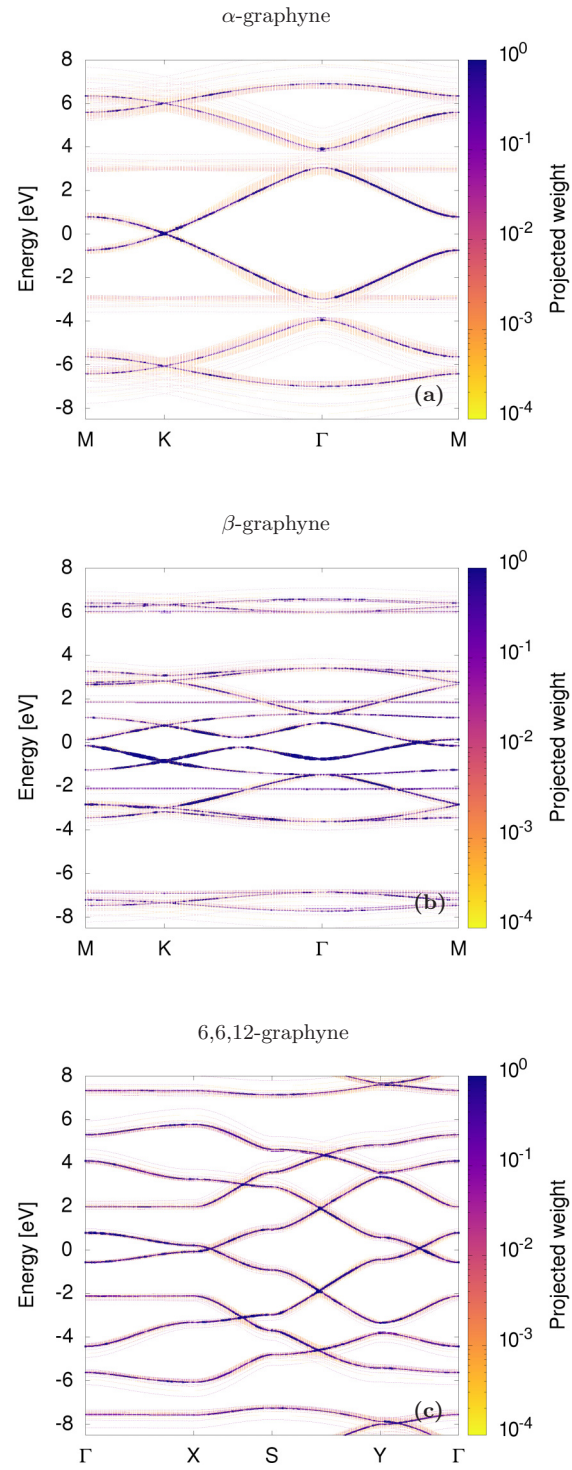

FIG. 4. Band manifolds in the extended zone scheme for α-graphyne, β-graphyne, and 6, 6, 12-graphyne. Shown is the projection of the wave function of the system with deformation onto the set of wave functions of the ideal system at $\mathbf{k}$, see Eq. (39), with the amplitude of the projection indicated by the color. These plots therefore represent the broadening of the eigenstates of the pristine material due to scattering induced by the deformation. By comparison with Fig. 2, which displays the band structures of the corresponding systems without deformation, we see that while the low-energy conical intersections are broadened by deformation, they are not significantly disrupted.

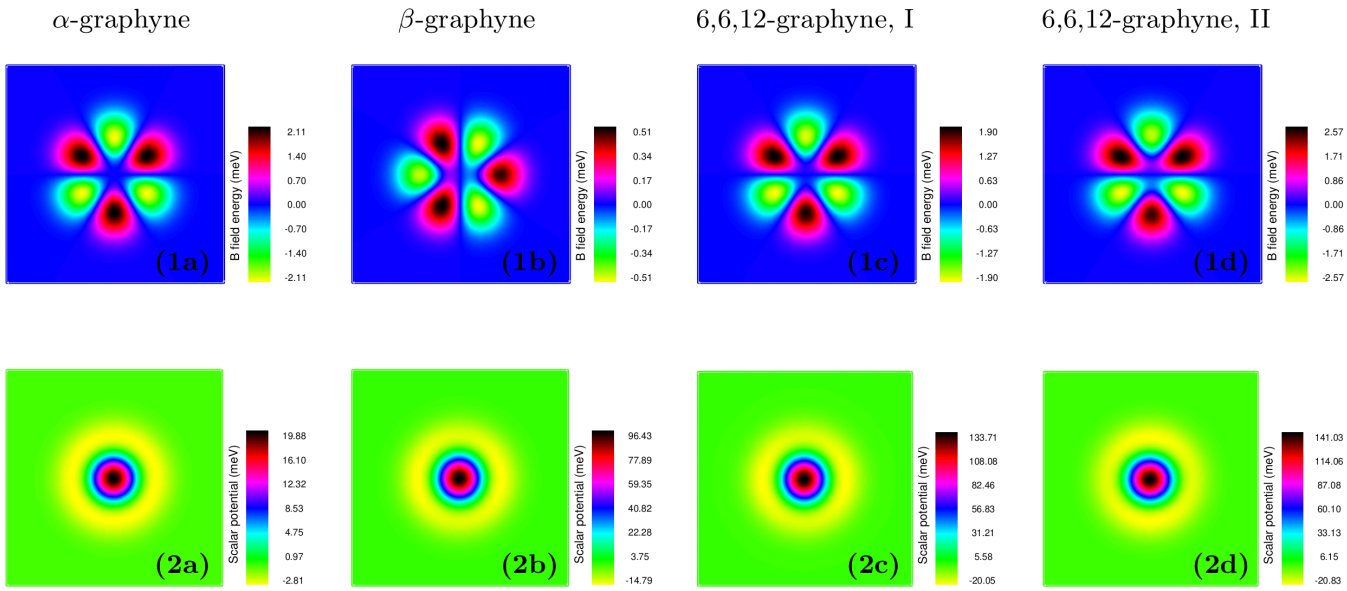

FIG. 5. Deformation induced magnetic fields in the graphynes. Shown are effective pseudomagnetic field and scalar potential generated by the deformation field displayed in Fig. 3, for α- and β-graphyne, and the two conical intersections of 6, 6, 12-graphyne. For ease of comparison, we present the magnetic field as an energy via multipliction of the Fermi velocity of each material. As can be seen, despite the very different lattice structures the effective fields induced by deformation are remarkably similar in form (the 90° rotation in β-graphyne is simply due to the fact the coordinate system is rotated by 90°).

the basis size is of between 1000 and 2000 states is usually sufficient for convergence. For further numerical details, we refer the reader to Ref. [47].

B. Spectral weight changes due to deformation

How are the band manifolds of the pristine lattices modified by deformation? As large scale periodic deformation results in a Brillouin zone reduced by a factor of 10^2–10^3 as compared to the pristine lattice, the multiplicity of backfolded and hybridized bands becomes very hard to interpret. A much more useful quantity is what could be called a "poor man's spectral function":

$$\omega(\mathbf{k},\epsilon) = \sum_j \rho_{\mathbf{k}j}\delta(\epsilon - \epsilon_{\mathbf{k}j}), \tag{39}$$

where

$$\rho_{\mathbf{k}j} = \sum_i \langle\phi_{\mathbf{k}i}|\Psi_{\mathbf{k}j}\rangle. \tag{40}$$

In this expression, $|\Psi_{\mathbf{k}j}\rangle$ is the jth eigenstate at crystal momentum $\mathbf{k}$ of the system with deformation and $|\phi_{\mathbf{k}i}\rangle$ an eigenstate, also at $\mathbf{k}$, for the system without deformation. In the absence of deformation $\rho_{\mathbf{k}j} = 1$ and Eq. (39) is simply the band structure of the pristine material. However, in the presence of deformation, $|\Psi_{\mathbf{k}j}\rangle$ will involve the coupling together of many eigenstates of the pristine system and $\rho_{\mathbf{k}j} < 1$. Thus Eq. (39) represents how the bands of the high-symmetry system are broadened through scattering induced by the deformation. To explore this we consider the deformation field shown in Fig. 3, similar to those typically employed in the discussion of nonuniform deformation in graphene. Panel (a) of this figure shows the deformation field, while panel (b) shows the magnitude of the deformation tensor is shown. The maximum value of the strain tensor is ∼7%; our *ab initio* calculations indicate that strains of <7% are within the elastic regime of these materials. As can be seen in Fig. 4 for each of the three graphynes, we consider the "spectral function" follows closely the band structures of the pristine systems (see Fig. 2) but with the expected deformation induced broadening. The nonuniform "speckled" nature of the spectral intensity along the band lines can be understood as arising from the complex multiple intersections and subsequent hybridization that occurs when the bands are folded back to the Brillouin zone of the deformed system; in the extended zone scheme, this will be manifested as a nonuniform spectral weight along the band lines.

C. Charge inhomogenity and current flow

Having established the robustness of the low-energy manifold to deformation, we now consider a description of deformation within a continuum theory of the low-energy conical intersection. In this case, the physics is encoded in the effective electric and pseudomagnetic fields that augment the Dirac-Weyl equation, and these fields are shown in Fig. 5 for α-, β- and 6, 6, 12-graphyne, each with the same circularly symmetric deformation field shown in Fig. 3. Strikingly, for all three materials the form of the effective pseudomagnetic and scalar fields is very similar. This is remarkable when one considers the very different lattice structures of these three systems, with α- and β-graphyne possessing hexagonal lattices and 6,6,12-graphyne a rectangular lattice. While the pseudomagnetic fields are comparable in magnitude, the scalar field is almost an order of magnitude greater for cone II of 6,6,12-graphyne than for α-graphyne suggesting that the interplay of gauge and scalar fields, known to be significant

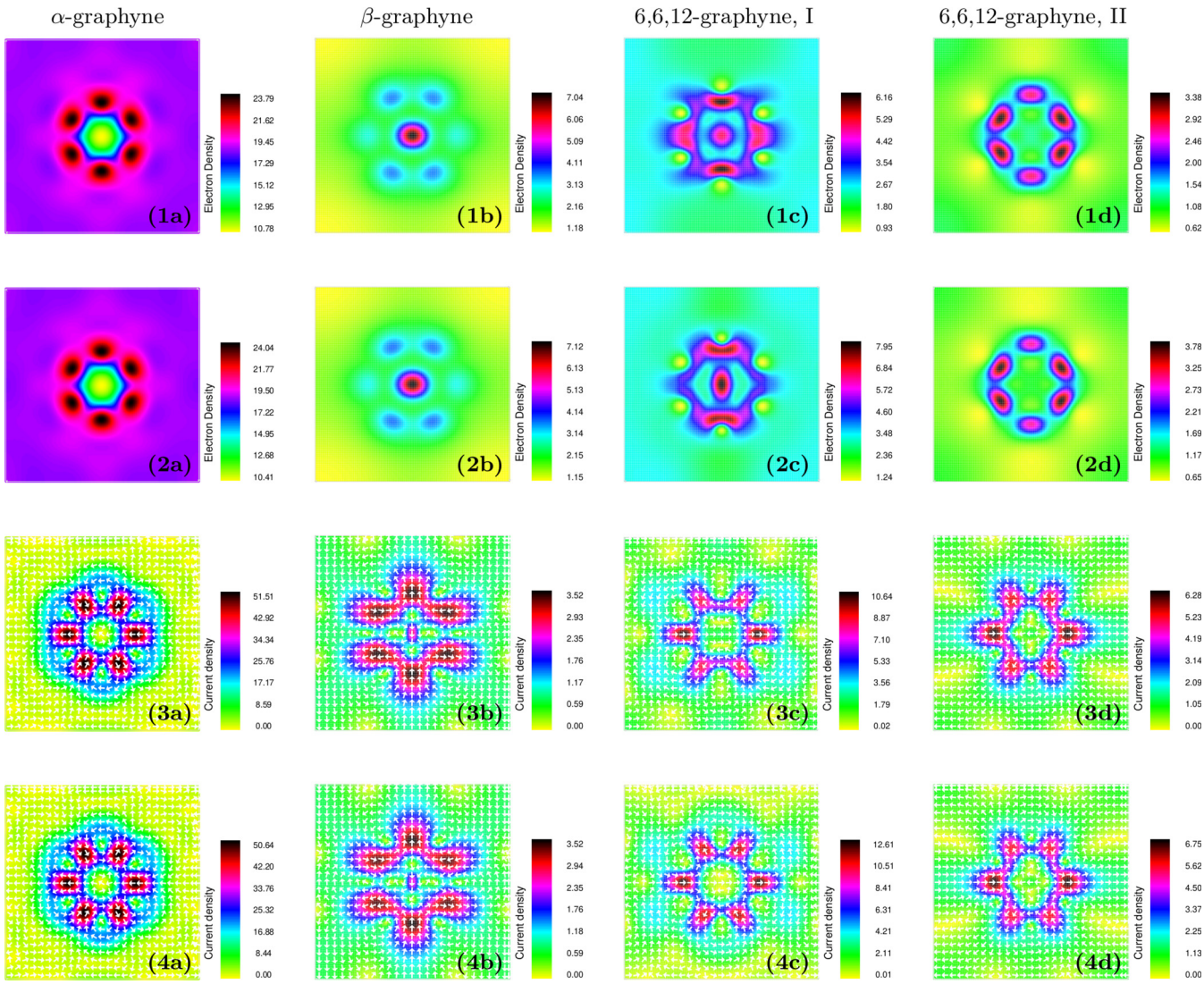

FIG. 6. Density and current density induced by the deformation in the graphynes. Shown in columns 1 to 4 are results for, respectively, α-graphyne, β-graphyne, the Dirac cone on the X-S symmetry line of 6, 6, 12-graphyne, and the Dirac cone that lies on the Γ-Y symmetry line of 6, 6, 12-graphyne. In each case, the deformation field is that given in Fig. 3. The energy window within which the density and current density are integrated is, 0–100 meV for α-graphyne, 0–10 meV for β-graphyne, and 20–30 meV at both conical intersections in 6, 6, 12-graphyne; similar results are however seen for any low-energy window. The units are Å^{-2} for the electron density and eV/Å for the current density; all densities and current densities are multiplied by the unit cell area $(100a)^2$. The first and second rows show the electron density generated by the two-band and full-band continuum pictures, respectively, while rows 3 and 4 show the current density produced by the two-band and all-band continuum theories, respectively. In all cases, it can be seen that the two-band and all-band continuum theories are in excellent agreement, and thus the Dirac-Weyl description of deformation remains valid for these materials, despite their complex lattice structures. While α-graphyne exhibits exactly the same "charge flowers" found in graphene, see (1a) and (2a) for the other graphynes this is not the case with, in particular, cone I of 6, 6, 12-graphyne, (1c) and (2c), clearly exhibiting the C_2 symmetry of the underlying lattice.

for describing nanobubbles in graphene, would be especially important in this material [3,61].

Is the two-band Dirac-Weyl theory of deformation valid in these more complex carbon architectures? To probe this question we now examine the deformation induced changes in electron density and current density calculated using the two-band and full-band continuum theories. If the Dirac-Weyl continuum theory provides a valid description, then results from these two distinct continuum theories should be in close agreement. Rows 1 and 2 of Fig. 6 show electron density using the two-band and full-band continuum theory, respectively, and rows 3 and 4 display the current density, again calculated from the two- and full-band continuum theory, respectively. For both density and current density, it can be seen that the results of the two continuum theories are in very good agreement: the Dirac-Weyl description of deformation thus remains valid for these much more complex lattice structures.

We now consider the structure of the deformation induced changes to electron density and current density. For α-graphyne these are very similar to those reported in previous studies of graphene for circularly symmetric deformation fields, with "charge flowers"[62] of C_6 symmetry and an

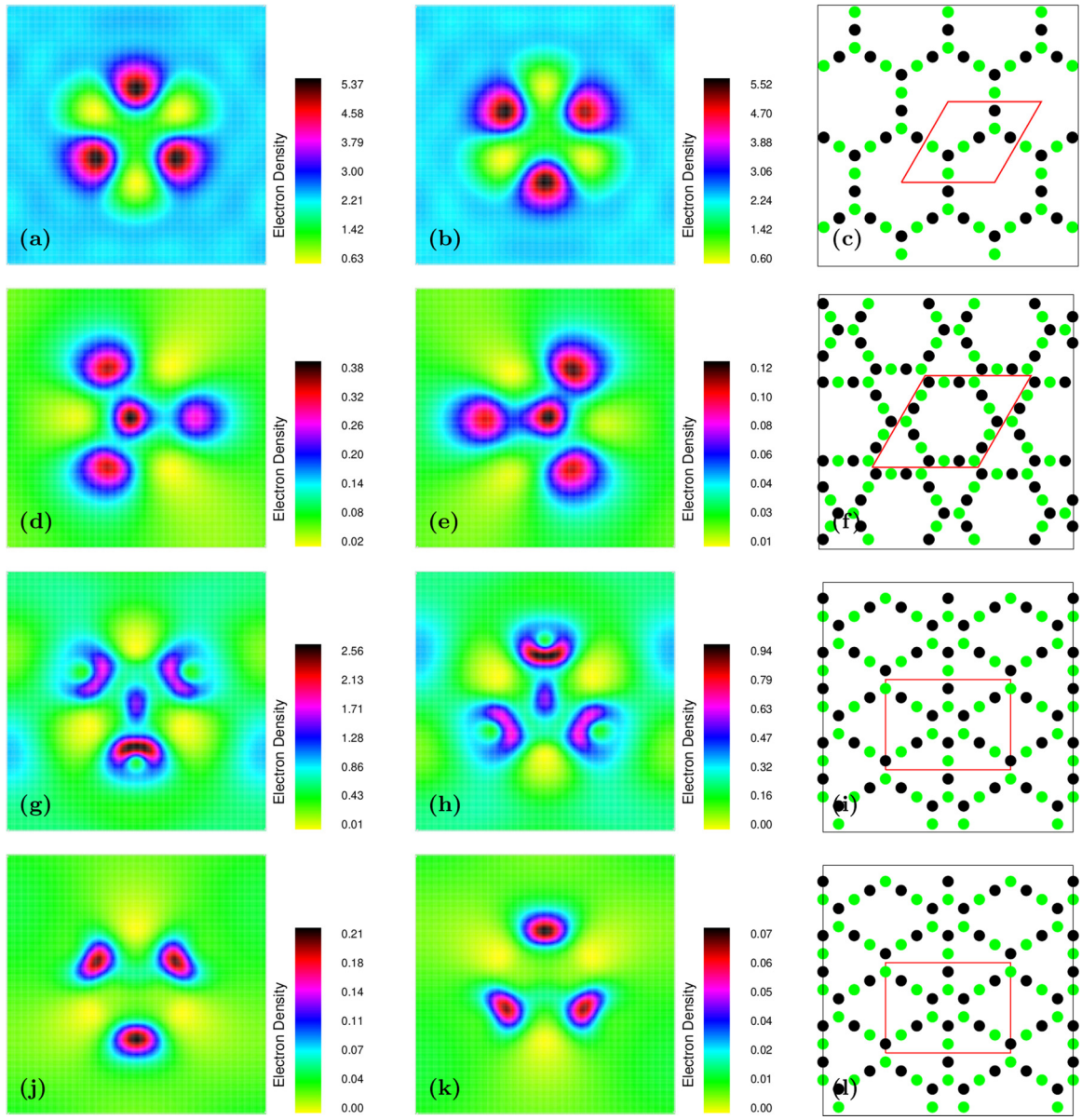

FIG. 7. Pseudospin polarization near the Dirac point in the graphynes. Each row shows the atom projected density for α-graphyne [(a) and (b)], β-graphyne [(d) and (e)], and cones I [(g) and (h)] and II [(j) and (k)] of 6, 6, 12-graphyne for the same deformation and integration window employed in Fig. 6. For all atoms in the unit cell of these materials, the atomic projected electron density takes on one of these two forms. The assignment of each atom in the unit cell to each of the two projection types is shown in the third column with the A and B type atoms, corresponding to columns one and two, respectively, shown by dark and light (green) shading, respectively. Pseudospin polarization due to deformation, well known in graphene, thus generalizes to the graphynes. As in Fig. 6, the units are Å^{-2} and densities are multiplied by the unit cell area $(100a)^2$.

associated C_3 symmetry current density pattern [63–65], see panels (1a)–(4a) of Fig. 6. For β- and 6, 6, 12-graphyne, however, the density exhibits a much lower symmetry, especially striking for cone I of 6,6,12-graphyne. This reflects the C_2 lattice symmetry for 6,6,12-graphyne. The corresponding current densities are, however, much closer in form to those found in α-graphyne and graphene.

As the effective fields induced by deformation showed no great distinction of form, the differences in electron density indicates the importance of the transformation from the pseudospinor of the Dirac-Weyl equation back to the physical wave function discussed in Sec. II. However, the deformation induced current densities do correspond to the pseudomagnetic fields shown in Fig. 5, with regions of strong current flow occurring at the nodal lines of the pseudomagnetic field. The current density induced by deformation in these graphynes can therefore, just as in graphene, be understood as due to snake states [63,64,66] at regions where the pseudomagnetic field changes sign.

Finally we examine the question of sublattice polarization. In graphene, the deformation induced charge density is strongly polarized on sublattice A or B, which can be viewed in the Dirac-Weyl picture as a local pseudospin polarization. The more complex lattice structures for α-, β-, and 6, 6, 12-

graphyne, which have 8, 18, and 18 atoms in the unit cell respectively, suggests that this physics will not be transferable to these more complex carbon architectures. Remarkably, as can be seen in Fig. 7, this is not the case. For each of these materials the atom projected density takes on one of only two forms, exhibited in the first two columns, with the correspondence between projection type and atom position in the unit cell shown in column three. However, while each of the 8 atoms of α-graphyne have a density given exactly by one of these two projection types, for β-graphyne and 6,6,12-graphyne, there are slight deviations amongst the nine atom projections of each type.

D. The role of optical deformation

Thus far we have not considered the role of local relaxations which will undoubtedly be induced by application of a deformation field. This is known to be more significant in these materials than in graphene (where it can also qualitatively change the physics [67]). In the case of graphene the two atom unit cell leads to a natural effective Hamiltonian theory in terms of acoustic and optical deformation fields, as recently discussed by Gupta *et al.* [47]. However, the more complex unit cells of the graphynes imply many more optical modes. To simplify this situation, and by analogy with graphene, we can define optical and acoustic modes in terms of the two groups of atoms on which charge is localized due to pseudospin polarization. In this way, we can define the average displacement of each group of atoms off their ideal positions under strain, and so define single optical and acoustic modes.

To investigate this, we have performed *ab initio* calculations for 6, 6, 12-graphyne using the VASP software suite [68,69], in which we allow the 18 atoms of the unit cell to relax under an applied biaxial strain. Figure 8 shows the magnitude of the resulting optical deformation, due to local atomic relaxation, given as a percentage of the nearest-neighbor separation for a range of biaxial strains. As can be seen, for biaxial strains of up to 6%, the optical deformation is of the order of 1%. Beyond 8% biaxial strain the lattice substantially reconstructs. Thus optical deformation will likely play some role in the physics of these materials, as they do with graphene, and may in principle be included in an effective Hamiltonian description following the scheme outlined in Ref. [47].

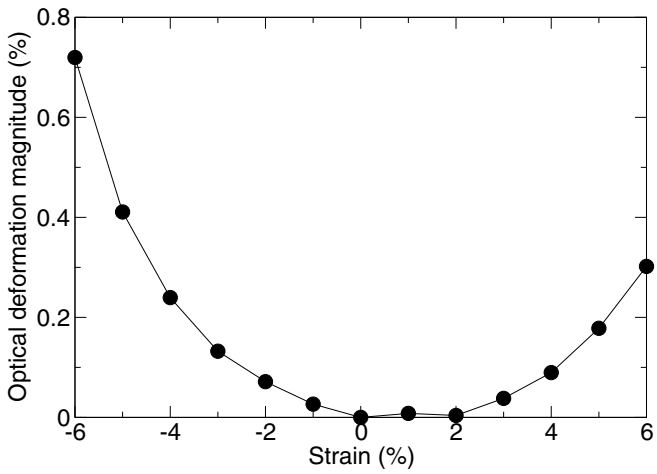

FIG. 8. Optical deformation due to local atomic relaxation induced by biaxial strain in 6,6,12-graphyne. For each group of atoms on which pseudospin polarization occurs (see Fig. 7), we define the average displacement of the atoms from their ideal positions under strain. From these two average displacements, the acoustic and optical components of the deformation then may be calculated and the deformation magnitude plotted as a function of applied strain. Note that the acoustic component, as expected, is zero.

V. DISCUSSION

The principal question we have addressed is whether the intuitive Dirac-Weyl description of deformation in graphene generalizes to the more complex carbon architectures of the graphynes. To answer this question, we have generalized the continuum theory of deformation in graphene to arbitrary numbers of sublattices, and considered this theory at two levels: a truncated Dirac-Weyl type theory, formally identical to that of graphene, and the full theory including all sublattice degrees of freedom (which therefore describes the full band structure and not only the low-energy conical intersection). For α-, β-, and 6, 6, 12-graphyne these two levels of theory lead to very similar results for the deformation induced changes to the density and current density close to the Dirac point, showing that the Dirac-Weyl description remains valid for these materials. Deformation in the graphynes thus retains the remarkable connection between structural change and pseudomagnetic and scalar fields found in graphene, and the rich physics of that material—valley filters [4–8], pseudospin polarization [9,10], and deformation induced Landau ladders [3]—can be expected to be found in the graphynes, if they can be synthesized.

ACKNOWLEDGMENT

This work was carried out in the framework of SFB 953 of the Deutsche Forschungsgemeinschaft (DFG).

APPENDIX: THE CONTINUITY EQUATION FOR DEFORMATION IN DIRAC-WEYL MATERIALS

As our focus here will be on deformation in materials with low-energy conical intersections, and the valley currents that deformation induces, it is useful to demonstrate that the current operator defined in the previous section indeed satisfies the continuity equation for such systems. To this end, we consider the most general form of the Dirac-Weyl equation augmented by deformation induced fields which, up to second order in momentum, is given by

$$H = A_i(\mathbf{r})\sigma_i + i\Gamma_i(\mathbf{r})\sigma_i + v_F^{ij}(\mathbf{r})\sigma_i p_j + iw_F^{ij}(\mathbf{r})\sigma_i p_j + \frac{1}{2!}M^{ijk}(\mathbf{r})\sigma_i p_j p_k. \tag{A1}$$

In this expression, the index i runs over the three Pauli matrices σ_0, σ_1, and σ_2 and the indices j and k over the two degrees of freedom of space. Thus there are two effective gauge field terms: $\mathbf{A} = (A_1, A_2)$, an imaginary gauge [70] that transforms as a field in the Dirac-Weyl equation under rotation

of the graphene lattice

$$\begin{pmatrix} 0 & \Gamma_x - i\Gamma_y \\ \Gamma_x + i\Gamma_y & 0 \end{pmatrix} \rightarrow \begin{pmatrix} 0 & (\Gamma_x - i\Gamma_y)e^{i\theta} \\ (\Gamma_x + i\Gamma_y)e^{-i\theta} & 0 \end{pmatrix}$$

and a real valued gauge [70–75] that does not transform as a field (a phase $e^{i2\theta}$ is instead acquired). In addition there are real and imaginary parts to the scalar potential, A_0 and Γ_0, respectively. At linear order in momentum, v_F^{ij} and w_F^{ij} are the real [70,71,73,74] and imaginary velocity tensors. Finally there is also a trigonal warping term M^{ijk}. Higher orders of momenta can be included in Eq. (A1) but, if Hermiticity is to be preserved, only by restricting the spatial fields to be slowly varying [47].

It is not immediately evident that Eq. (A1) satisfies the continuity equation $\nabla \cdot \mathbf{j}(\mathbf{r}) + \partial_t n(\mathbf{r}) = 0$ (as both the Hamiltonians $v_F \boldsymbol{\sigma} \cdot \mathbf{p}$ and $v_F \boldsymbol{\sigma} \cdot \mathbf{p} + \sigma_i A_i$ obviously do) due both to the presence of the coordinate dependent velocity and mass tensors, as well as the fact that both gauge and velocity terms have both real and imaginary parts. However, as we now show using conditions that guarantee hermiticity of the deformation Hamiltonian, the continuity equation is indeed satisfied.

The jth component of the corresponding current operator is given by

$$j_j = v_F^{ij}(\mathbf{r})\sigma_i + i w_F^{ij}(\mathbf{r})\sigma_i + M^{ijk}(\mathbf{r})\sigma_i p_j \tag{A2}$$

with the divergence of the current density then given by

$$\begin{aligned} \nabla \cdot \mathbf{j}(\mathbf{r}) = \frac{1}{i\hbar}\Im[&(p_j\Psi)^\dagger v^{ij}\sigma_i\Psi - \Psi^\dagger v^{ij}\sigma_i p_j\Psi \\ &- \Psi^\dagger p_j v^{ij}\sigma_i\Psi + i(p_j\Psi)^\dagger w^{ij}\sigma_i\Psi \\ &- i\psi^\dagger w^{ij}\sigma_i p_j\Psi - i\Psi^\dagger p_j w^{ij}\sigma_i\Psi \\ &+ (p_j\Psi)^\dagger M^{ijk}\sigma_i p_j\Psi - \psi^\dagger M^{ijk}\sigma_i p_j p_k\Psi \\ &- \Psi^\dagger p_j M^{ijk}\sigma_i p_k\Psi]. \end{aligned}$$

Using the obvious relations $\Im[(p_j\Psi)^\dagger M^{ijk}\sigma_i p_j\Psi] = 0$ and $(\psi^\dagger v^{ij}\sigma_i p_j\Psi)^\dagger = (v^{ij}\sigma_i p_j\Psi)^\dagger\Psi$ in conjunction with the hermiticity conditions obeyed by the Hamiltonian [47,70]

$$p_j M^{ijk}\sigma_i p_k - 2i w^{ij}\sigma_i p_j = 0, \tag{A3}$$

$$p_j v^{ij}\sigma_i - 2i\Gamma_i\sigma_i = 0, \tag{A4}$$

we have

$$\nabla \cdot \mathbf{j}(\mathbf{r}) = \frac{1}{i\hbar}\Im[-2\Psi^\dagger H\Psi] \tag{A5}$$

and using

$$\partial_t n(\mathbf{r}) = \frac{1}{i\hbar}[\Psi^\dagger(H\Psi) - (H\Psi)^\dagger\Psi] \tag{A6}$$

we then find

$$\partial_t n(\mathbf{r}) + \nabla \cdot \mathbf{j}(\mathbf{r}) = 0, \tag{A7}$$

and so the continuity equation is satisfied.

[1] D. Moldovan, M. Ramezani Masir, and F. M. Peeters, Electronic states in a graphene flake strained by a gaussian bump, Phys. Rev. B **88**, 035446 (2013).

[2] M. A. H. Vozmediano, M. I. Katsnelson, and F. Guinea, Gauge fields in graphene, Phys. Rep. **496**, 109 (2010).

[3] N. Levy, S. A. Burke, K. L. Meaker, M. Panlasigui, A. Zettl, F. Guinea, A. H. C. Neto, and M. F. Crommie, Strain-induced pseudo–magnetic fields greater than 300 tesla in graphene nanobubbles, Science **329**, 544 (2010).

[4] T. Fujita, M. B. A. Jalil, and S. G. Tan, Valley filter in strain engineered graphene, Appl. Phys. Lett. **97**, 043508 (2010).

[5] M. Settnes, S. R. Power, M. Brandbyge, and A.-P. Jauho, Graphene Nanobubbles as Valley Filters and Beam Splitters, Phys. Rev. Lett. **117**, 276801 (2016).

[6] D. Zhai and N. Sandler, Local versus extended deformed graphene geometries for valley filtering, Phys. Rev. B **98**, 165437 (2018).

[7] F. Zhai, Y. Ma, and Y.-T. Zhang, A valley-filtering switch based on strained graphene, J. Phys.: Condens. Matter **23**, 385302 (2011).

[8] F. Zhai, X. Zhao, K. Chang, and H. Q. Xu, Magnetic barrier on strained graphene: A possible valley filter, Phys. Rev. B **82**, 115442 (2010).

[9] A. Georgi, P. Nemes-Incze, R. Carrillo-Bastos, D. Faria, S. Viola Kusminskiy, D. Zhai, M. Schneider, D. Subramaniam, T. Mashoff, N. M. Freitag, M. Liebmann, M. Pratzer, L. Wirtz, C. R. Woods, R. V. Gorbachev, Y. Cao, K. S. Novoselov, and N. Sandler, M. Morgenstern, Tuning the pseudospin polarization of graphene by a pseudomagnetic field, Nano Lett. **17**, 2240 (2017).

[10] M. Settnes, S. R. Power, and A.-P. Jauho, Pseudomagnetic fields and triaxial strain in graphene, Phys. Rev. B **93**, 035456 (2016).

[11] J. Cao, C. P. Tang, and S.-J. Xiong, Analytical dispersion relations of three graphynes, Physica B (Amsterdam) **407**, 4387 (2012).

[12] N. Han, H. Liu, S. Zhou, and J. Zhao, Possible formation of graphyne on transition metal surfaces: A competition with graphene from the chemical potential point of view, J. Phys. Chem. C **120**, 14699 (2016).

[13] Y. Hang, W. Wen-Zhi, J. Yu, and W.-L. Guo, Tuning the energy gap of bilayer α-graphyne by applying strain and electric field, Chin. Phys. B **25**, 023102 (2016).

[14] H. Huang, W. Duan, and Z. Liu, The existence/absence of dirac cones in graphynes, New J. Phys. **15**, 023004 (2013).

[15] A. L. Ivanovskii, Graphynes and graphdyines, Prog. Solid State Chem. **41**, 1 (2013).

[16] J. Kang, Z. Wei, and J. Li, Graphyne and its family: Recent theoretical advances, ACS Appl. Mater. Interfaces **11**, 2692 (2019).

[17] H. Kim, Y. Kim, J. Kim, and W. Y. Kim, Computational searching for new stable graphyne structures and their electronic properties, Carbon **98**, 404 (2016).

[18] Z. Li, Z. Liu, and Z. Liu, Movement of dirac points and band gaps in graphyne under rotating strain, Nano Res. **10**, 2005 (2017).

[19] Z. Liu, G. Yu, H. Yao, L. Liu, L. Jiang, and Y. Zheng, A simple tight-binding model for typical graphyne structures, New J. Phys. **14**, 113007 (2012).

[20] D. Malko, C. Neiss, F. Viñes, and A. Görling, Competition for Graphene: Graphynes with Direction-Dependent Dirac cones, Phys. Rev. Lett. **108**, 086804 (2012).

[21] K. M. Merz, R. Hoffmann, and A. T. Balaban, 3, 4-connected carbon nets: Through-space and through-bond interactions in the solid state, J. Am. Chem. Soc. **109**, 6742 (1987).

[22] J. E. Padilha, A. Fazzio, and A. J. R. da Silva, Directional control of the electronic and transport properties of graphynes, J. Phys. Chem. C **118**, 18793 (2014).

[23] M. Park, Y. Kim, and H. Lee, Design of 2D massless Dirac fermion systems and quantum spin Hall insulators based on sp–sp2 carbon sheets, npj Comput. Mater. **4**, 54 (2018).

[24] Q. Peng, W. Ji, and S. De, Mechanical properties of graphyne monolayers: A first-principles study, Phys. Chem. Chem. Phys. **14**, 13385 (2012).

[25] Q. Peng, A. K. Dearden, J. Crean, L. Han, S. Liu, X. Wen, and S. De, New materials graphyne, graphdiyne, graphone, and graphane: Review of properties, synthesis, and application in nanotechnology, Nanotechnol., Sci. Appl. **7**, 1 (2014).

[26] H. R. Soni and P. K. Jha, Vibrational and elastic properties of 2d carbon allotropes: A first principles study, Solid State Commun. **189**, 58 (2014).

[27] Y. Tian, Z. Li, and K. Cai, Wrinkling behavior of annular graphynes under circular shearing load using molecular dynamics simulations, Nanomaterials Nanotechnol. **5**, 9 (2015).

[28] G. van Miert and C. M. Smith, Dirac cones beyond the honeycomb lattice: A symmetry-based approach, Phys. Rev. B **93**, 035401 (2016).

[29] G. van Miert, V. Juričić, and C. Morais Smith, Tight-binding theory of spin-orbit coupling in graphynes, Phys. Rev. B **90**, 195414 (2014).

[30] G. van Miert, C. M. Smith, and V. Juričić, High-chern-number bands and tunable dirac cones in β-graphyne, Phys. Rev. B **90**, 081406 (2014).

[31] J. Wang, H. Huang, W. Duan, and Z. Liu, Identifying dirac cones in carbon allotropes with square symmetry, J. Chem. Phys. **139**, 184701 (2013).

[32] J. Wang, S. Deng, Z. Liu, and Z. Liu, The rare two-dimensional materials with dirac cones, National Sci. Rev. **2**, 22 (2015).

[33] L.-C. Xu, R.-Z. Wang, M.-S. Miao, X.-L. Wei, Y.-P. Chen, H. Yan, W.-M. Lau, L.-M. Liu, and Y.-M. Ma, Two dimensional dirac carbon allotropes from graphene, Nanoscale **6**, 1113 (2014).

[34] Y.-G. Xu, C. Ming, Z.-Z. Lin, F.-X. Meng, J. Zhuang, and X.-J. Ning, Can graphynes turn into graphene at room temperature? Carbon **73**, 283 (2014).

[35] D. Z. Yang, M. S. Si, G. P. Zhang, and D. S. Xue, Crystal momentum-dependent anisotropy of the dirac cone in the rectangular carbon allotropes, Europhys. Lett. **107**, 20003 (2014).

[36] L. Yi, Y. Zhang, X. Feng, T. Chang, J. Wang, J. Du, and J. Zhou, Mechanical properties of graphynes under shearing and bending, J. Appl. Phys. **119**, 204304 (2016).

[37] Q. Yue, S. Chang, J. Kang, S. Qin, and J. Li, Mechanical and electronic properties of graphyne and its family under elastic strain: Theoretical predictions, J. Phys. Chem. C **117**, 14804 (2013).

[38] Q. Zhang, C. Tang, W. Zhu, and C. Cheng, Strain-enhanced li storage and diffusion on the graphyne as the anode material in the li-ion battery, J. Phys. Chem. C **122**, 22838 (2018).

[39] S. Zhang, J. Wang, Z. Li, R. Zhao, L. Tong, Z. Liu, J. Zhang, and Z. Liu, Raman spectra and corresponding strain effects in graphyne and graphdiyne, J. Phys. Chem. C **120**, 10605 (2016).

[40] Y. Y. Zhang, Q. X. Pei, and C. M. Wang, Mechanical properties of graphynes under tension: A molecular dynamics study, Appl. Phys. Lett. **101**, 081909 (2012).

[41] Jia-Jia Zheng, Xiang Zhao, Yuliang Zhao, and Xingfa Gao, Two-Dimensional Carbon Compounds Derived from Graphyne with Chemical Properties Superior to Those of Graphene, Sci. Rep. **3**, 1271 (2013).

[42] Y. Li, L. Xu, H. Liu, and Y. Li, Graphdiyne and graphyne: From theoretical predictions to practical construction, Chem. Soc. Rev. **43**, 2572 (2014).

[43] Z. Li, M. Smeu, A. Rives, V. Maraval, R. Chauvin, M. A. Ratner, and E. Borguet, Towards graphyne molecular electronics, Nat. Commun. **6**, 6321 (2015).

[44] A. R. Puigdollers, G. Alonso, and P. Gamallo, First-principles study of structural, elastic and electronic properties of α-, β- and γ-graphyne, Carbon **96**, 879 (2016).

[45] G. Wang, M. Si, A. Kumar, and R. Pandey, Strain engineering of dirac cones in graphyne, Appl. Phys. Lett. **104**, 213107 (2014).

[46] Z. Li, J. Wang, and Z. Liu, Intrinsic carrier mobility of dirac cones: The limitations of deformation potential theory, J. Chem. Phys. **141**, 144107 (2014).

[47] R. Gupta, F. Rost, M. Fleischmann, S. Sharma, and S. Shallcross, Straintronics beyond homogeneous deformation, Phys. Rev. B **99**, 125407 (2019).

[48] F. Kisslinger, C. Ott, C. Heide, E. Kampert, B. Butz, E. Spiecker, S. Shallcross, and H. B. Weber, Linear magnetoresistance in mosaic-like bilayer graphene, Nat. Phys. **11**, 650 (2015).

[49] N. Ray, F. Rost, D. Weckbecker, M. Vogl, S. Sharma, R. Gupta, O. Pankratov, and S. Shallcross, Going beyond $k \cdot p$ theory: a general method for obtaining effective Hamiltonians in both high and low symmetry situations, arXiv:1607.00920.

[50] F. Rost, R. Gupta, M. Fleischmann, D. Weckbecker, N. Ray, J. Olivares, M. Vogl, S. Sharma, O. Pankratov, and S. Shallcross, Nonperturbative theory of effective hamiltonians for deformations in two-dimensional materials: Moiré systems and dislocations, Phys. Rev. B **100**, 035101 (2019).

[51] S. Shallcross, S. Sharma, and B. H. Weber, Anomalous dirac point transport due to extended defects in bilayer graphene, Nat. Commun. **8**, 342 (2017).

[52] D. Weckbecker, R. Gupta, F. Rost, S. Sharma, and S. Shallcross, Dislocation and node states in bilayer graphene systems, Phys. Rev. B **99**, 195405 (2019).

[53] T. B. Boykin, M. Luisier, and G. Klimeck, Eur. J. Phys. **31**, 1077 (2010).

[54] T. N. Todorov, J. Phys.: Condens. Matter **14**, 3049 (2002).

[55] I. Paul and G. Kotliar, Thermal transport for many-body tight-binding models, Phys. Rev. B **67**, 115131 (2003).

[56] H.-T. Yang and C. Liu, Description of spin transport and precession in spin-orbit coupling systems and general equation of continuity, Phys. Rev. B **75**, 085314 (2007).

[57] F. M. D. Pellegrino, G. G. N. Angilella, and R. Pucci, Transport properties of graphene across strain-induced nonuniform velocity profiles, Phys. Rev. B **84**, 195404 (2011).

[58] F. Bottegoni, H.-J. Drouhin, G. Fishman, and J.-E. Wegrowe, Probability- and spin-current operators for effective hamiltonians, Phys. Rev. B **85**, 235313 (2012).

[59] F. Bottegoni, H.-J. Drouhin, J.-E. Wegrowe, and G. Fishman, Probability-current definition in presence of spin-orbit interaction, J. Appl. Phys. **111**, 07 (2012).

[60] C. Schnittler and M. Kirilov, Hamiltonian and Boundary Conditions for Electrons in Semiconductor Heterostructures, Phys. Status Solidi B **176**, 143 (1993).

[61] E. V. Castro, M. A. Cazalilla, and M. A. H. Vozmediano, Raise and collapse of pseudo landau levels in graphene, Phys. Rev. B **96**, 241405 (2017).

[62] R. Carrillo-Bastos, D. Faria, A. Latgé, F. Mireles, and N. Sandler, Gaussian deformations in graphene ribbons: Flowers and confinement, Phys. Rev. B **90**, 041411 (2014).

[63] D. Faria, A. Latgé, S. E. Ulloa, and N. Sandler, Currents and pseudomagnetic fields in strained graphene rings, Phys. Rev. B **87**, 241403 (2013).

[64] G. M. M. Wakker, R. P. Tiwari, and M. Blaauboer, Localization and circulating currents in curved graphene devices, Phys. Rev. B **84**, 195427 (2011).

[65] H.-T. Yang, Potential-driven eddy current in rippled graphene nanoribbons, arXiv:1210.1727v2.

[66] J. Reijniers and F. M. Peeters, Snake orbits and related magnetic edge states, J. Phys.: Condens. Matter **12**, 9771 (2000).

[67] T. O. Wehling, A. V. Balatsky, A. M. Tsvelik, M. I. Katsnelson, and A. I. Lichtenstein, Midgap states in corrugated graphene: Ab initio calculations and effective field theory, Europhys. Lett. **84**, 17003 (2008).

[68] G. Kresse and J. Furthmüller, Efficient iterative schemes for ab initio total-energy calculations using a plane-wave basis set, Phys. Rev. B **54**, 11169 (1996).

[69] G. Kresse and J. Furthmüller, Efficiency of ab-initio total energy calculations for metals and semiconductors using a plane-wave basis set, Comput. Mater. Sci. **6**, 15 (1996).

[70] F. de Juan, M. Sturla, and M. A. H. Vozmediano, Space Dependent Fermi Velocity in Strained Graphene, Phys. Rev. Lett. **108**, 227205 (2012).

[71] B. Amorim, A. Cortijo, F. de Juan, A. G. Grushin, F. Guinea, A. Gutiérrez-Rubio, H. Ochoa, V. Parente, R. Roldán, P. San-Jose, J. Schiefele, M. Sturla, and M. A. H. Vozmediano, Novel effects of strains in graphene and other two dimensional materials, Phys. Rep. **617**, 1 (2016).

[72] J. L. Mañes, Symmetry-based approach to electron-phonon interactions in graphene, Phys. Rev. B **76**, 045430 (2007).

[73] M. R. Masir, D. Moldovan, and F. M. Peeters, Pseudo magnetic field in strained graphene: Revisited, Solid State Commun. **175-176**, 76 (2013); Special Issue: Graphene V: Recent Advances in Studies of Graphene and Graphene analogues.

[74] M. Oliva-Leyva and G. G. Naumis, Generalizing the fermi velocity of strained graphene from uniform to nonuniform strain, Phys. Lett. A **379**, 2645 (2015).

[75] H. Suzuura and T. Ando, Phonons and electron-phonon scattering in carbon nanotubes, Phys. Rev. B **65**, 235412 (2002).